

RASLF: Representation-Aware State Space Model for Light Field Super-Resolution

Zeqiang Wei, Kai Jin, Kuan Song, Xiuzhuang Zhou, Wenlong Chen, Min Xu*

Abstract—Current SSM-based light field super-resolution (LFSR) methods often fail to fully leverage the complementarity among various LF representations, leading to the loss of fine textures and geometric misalignments across views. To address these issues, we propose RASLF, a representation-aware state-space framework that explicitly models structural correlations across multiple LF representations. Specifically, a Progressive Geometric Refinement (PGR) block is created that uses a panoramic epipolar representation to explicitly encode multi-view parallax differences, thereby enabling integration across different LF representations. Furthermore, we introduce a Representation-Aware Asymmetric Scanning (RAAS) mechanism that dynamically adjusts scanning paths based on the physical properties of different representation spaces, optimizing the balance between performance and efficiency through path pruning. Additionally, a Dual-Anchor Aggregation (DAA) module improves hierarchical feature flow, reducing redundant deep-layer features and prioritizing important reconstruction information. Experiments on various public benchmarks show that RASLF achieves the highest reconstruction accuracy while remaining highly computationally efficient.

Index Terms—light field image processing, image super-resolution

I. INTRODUCTION

LIGHT field (LF) imaging captures both the spatial intensity and angular information of light rays, offering rich geometric priors that facilitate various downstream applications, including depth estimation [1], [2] and refocusing [3], [4]. However, the physical constraints of imaging sensors create an inherent trade-off between spatial and angular resolutions, usually resulting in sub-aperture images (SAIs) with limited spatial detail. Therefore, light field super-resolution (LFSR) focuses on reconstructing high-quality details from low-resolution data, with the main challenge being to recover high-frequency textures while maintaining strict geometric consistency across views within the inherent spatial-angular structure.

Recently, SSMs [5] have been introduced into LFSR to leverage linear computational complexity and model long-range dependencies, demonstrating promising effectiveness. Unlike CNNs, limited by local receptive fields, and Transformers, burdened by quadratic complexity, SSMs are theoretically

better at capturing long-range spatial-angular correlations in high-dimensional LF data.

Despite these advantages, current SSM-based LFSR methods [6]–[8] still find it challenging to effectively capitalize on the diverse representations of LF data. Specifically, many approaches limit their focus to a single LF domain, thereby overlooking the structural complementarity offered by other representations. Even for methods that aim to incorporate multiple representations, the lack of a robust modeling framework often leads to heuristic aggregation that doesn't explicitly capture complex cross-view dependencies and long-range spatial-angular correlations.

Motivated by recent findings [9]–[11] that multi-directional scanning in image-based SSMs often induces feature redundancy, we observe that existing SSM-based LFSR methods typically adopt a representation-agnostic configuration that uses a uniform set of scanning paths for all LF representations. Such designs ignore the inherent structural differences among LF representations. For instance, spatial-angular textures usually exhibit more balanced dependencies across different directions and therefore benefit from multi-directional scanning, whereas epipolar lines follow clear directional trajectories, making some scanning paths unnecessary. Therefore, a uniform scanning strategy causes unnecessary computational overhead and reduces feature focus in highly structured LF representations.

To overcome these limitations, we introduce RASLF, a representation-aware state-space framework designed for LFSR. Specifically, we developed a Progressive Geometric Refinement (PGR) block that leverages a Panoramic Epipolar Representation to transform fragmented observations into a globally coherent geometric space, facilitating explicit parallax-aware feature interaction. Building on this, a Representation-Aware Asymmetric Scanning (RAAS) strategy is introduced to align sequential modeling trajectories with the structural characteristics of different LF representations, thereby reducing computational redundancy while reinforcing geometric constraints. Moreover, a Dual-Anchor Aggregation (DAA) module is incorporated to regulate hierarchical feature propagation, thereby filtering deep-layer redundancy and focusing computational budget on reconstruction-critical cues. Extensive evaluations confirmed that RASLF offers a better balance between reconstruction accuracy and computational efficiency across multiple benchmarks.

In summary, our primary contributions are as follows:

- 1) We proposed a Progressive Geometric Refinement (PGR) block and a Panoramic Epipolar Representation, which jointly transform fragmented local constraints into a glob-

Corresponding author: Min Xu.

Zeqiang Wei, Min Xu, and Wenlong Chen are with the Capital Normal University Information Engineering College, Beijing 100048, China (email: weizeqiang@cnu.edu.cn, xumin@cnu.edu.cn, chenwenlong@cnu.edu.cn). Kai Jin is with the Bigo Technology Pte. Ltd., Beijing 100020, China (email: jinkai@bigo.sg). Kuan Song is with the Explorer Global (Suzhou) Artificial Intelligence Technology Co., Ltd., Suzhou, Jiangsu 215123, China (email: songkuan@explorer.global). Xiuzhuang Zhou are with Beijing University of Posts and Telecommunications, Beijing 100088, China (email: xiuzhuang.zhou@bupt.edu.cn).

ally coherent geometric structure, significantly enhancing cross-view consistency.

- 2) We designed a Representation-Aware Asymmetric Scanning (RAAS) strategy that aligns sequential modeling paths with the physical and structural characteristics of diverse LF representations, thereby reducing redundancy and computational overhead.
- 3) To further improve feature utilization, we designed a Dual-Anchor Aggregation (DAA) module to optimize hierarchical feature propagation and suppress redundancy along the network hierarchy.
- 4) The proposed RASLF achieves a state-of-the-art (SOTA) balance between reconstruction quality and inference efficiency, as validated by extensive experiments on public LF datasets.

II. RELATED WORK

A. Light Field Representations

Light field data is typically parameterized as a 4D function $L(u, v, x, y)$, following the two-plane parameterization [12]. Here, (u, v) denotes the angular coordinates of the camera array, and (x, y) represents the spatial coordinates within each view. This high-dimensional structure captures both spatial textures and angular correlations, which can be broken down into three functionally distinct 2D representations:

- Sub-Aperture Images (SAI): By fixing the angular coordinates at (u, v) , an SAI $I_{u,v}(x, y)$ is obtained. SAIs resemble traditional 2D images and are primarily used to extract spatial features.
- Macro-Pixel Images (MacPI): A MacPI $I_{x,y}(u, v)$ is formed by gathering pixels from all viewpoints at a fixed spatial location (x, y) . It encapsulates the angular distribution of light rays.
- Epipolar Plane Images (EPI): By fixing one spatial and one angular dimension, the EPI $I_{y,v}(x, u)$ or $I_{x,u}(y, v)$ is generated. Since the parallax of a scene point is proportional to its depth, scene objects appear as directional linear structures with different slopes in EPIs [13]. This structural anisotropy defines EPIs as the primary domain for enforcing geometric consistency.

In the LFSR task, these three representations provide different but complementary viewpoints. Early methods [14], [15] predominantly performed spatial super-resolution on independent SAIs, a practice that treats the light field as a set of isolated 2D images while ignoring angular consistency. To establish cross-dimensional correlations, spatial-angular interaction paradigms were developed to model the relationship between spatial textures and angular distributions by synergistically leveraging SAIs and MacPIs. To further ensure geometric consistency, subsequent research introduced explicit EPI-based constraints on parallax slopes, yielding multi-representation frameworks that integrate spatial, angular, and epipolar information.

B. Methods based on Spatial-Angular Interaction

Spatial-angular interaction methods circumvent the high complexity of direct 4D processing by decomposing feature

extraction into dimensionally decoupled 2D operations. LF-InterNet [16] utilizes parallel branches to iteratively exchange spatial and angular information. To mitigate parallax-induced misalignments inherent in decoupled paradigms, LF-DFnet [17] introduced the Angular Deformable Alignment Module (ADAM) for non-rigid feature warping, while LF-IINet [18] refined interactions via parallel intra-inter view branches. HDDRNet [19] further simulated 4D correlations by using dense residual connections between the SAI and MacPI representations to enable intensive feature reuse. However, the localized receptive fields of CNNs preclude the capture of long-range dependencies across distant viewpoints or large spatial structures.

To overcome this, transformer-based architectures utilize self-attention mechanisms to aggregate global context. LFT [20] implements this through alternating spatial and angular Transformer modules, while DPT [21] and M2MT [22] utilize specialized attention blocks to aggregate many-to-many viewpoint priors. Despite their representational power, the quadratic computational complexity of self-attention leads to excessive computational and memory overhead. Most recently, State Space Models (SSM), particularly Mamba-based architectures, have emerged to provide global interaction with linear complexity.

Recent State Space Models (SSM), such as L^2 FMamba [8] and LFTransMamba [23], use selective scanning on serialized SAI and MacPI tokens, while MLFSR [6] ensures consistency through bi-directional subspace scanning. However, since these spatial-angular interaction methods rely on implicit feature-level correlations rather than explicit epipolar geometry constraints, they often struggle to maintain strict geometric consistency. Crucially, these approaches typically employ symmetric quad-directional scanning across all domains, which overlooks the structural anisotropy inherent in different LF representations. The lack of domain-specific physical priors in a uniform scanning technique results in considerable computational redundancy and diminishes the effectiveness of high-dimensional geometric modeling.

C. Methods based on Geometric Consistency

Enforcing explicit geometric constraints is essential for maintaining the structural integrity of LFSR. EPIT [24] tokenizes the EPI into several EPI-strips to characterize the non-local properties of epipolar geometry. By applying self-attention mechanisms within these stripes, the model effectively models the parallax continuity of long-range geometric structures.

Furthermore, to improve the geometric consistency of spatial-angular interactions, incorporating EPI geometric constraints via multi-representation learning has become a common approach. Based on the organizational structure of these representations, existing methods can be classified into parallel, sequential, and cascade paradigms.

The parallel paradigm, pioneered by the disentangled learning framework in DistgSSR [25], utilizes separate branches for spatial, angular, and epipolar features to independently extract domain-specific information before fusion. LFMamba

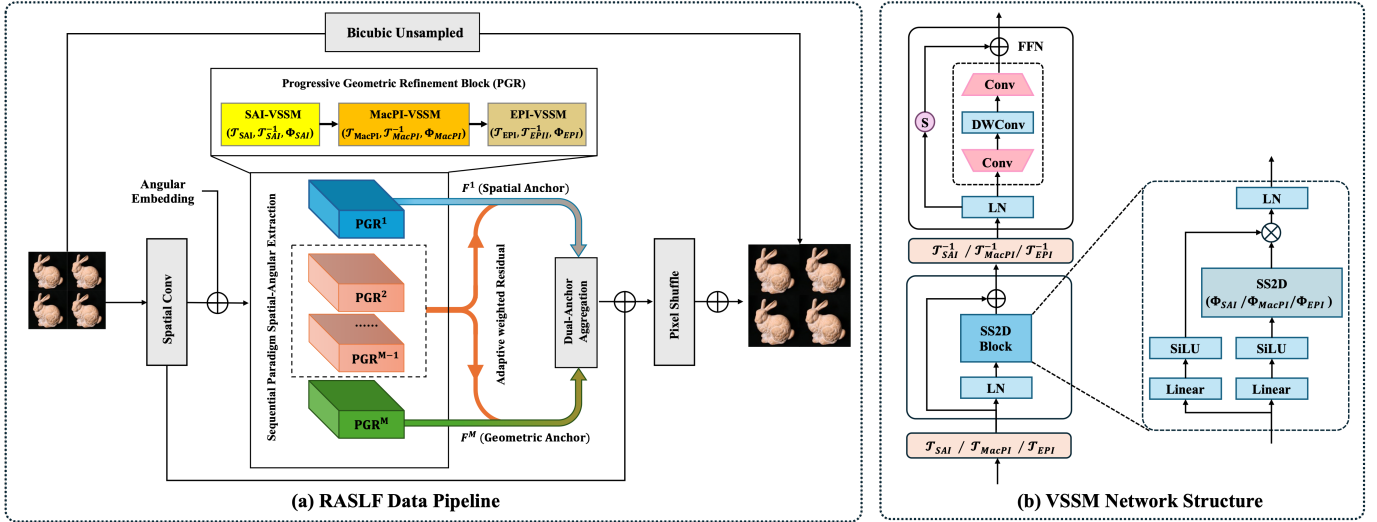


Fig. 1. Overall architecture of the proposed RASLF. (a) The Progressive Geometric Refinement (PGR) paradigm sequentially refines features using representation-specific VSSM units, and a Dual-Anchor Aggregation module fuses multi-stage features via spatial and geometric anchors. (b) Representation-Aware Asymmetric Scanning (RAAS) tailors SS2D scanning paths Φ and representation transforms $\mathcal{T}, \mathcal{T}^{-1}$ for SAI, MacPI, and EPI, reducing redundant computation while preserving geometry-aware dependencies.

[7] further advanced this architecture by incorporating Mamba into these parallel branches to capture long-range dependencies with linear complexity. However, such parallel processing often leads to feature redundancy and resource waste because features are extracted independently across domains.

The sequential paradigm prioritizes spatial-angular interaction over the integration of epipolar geometric constraints [26]–[28]. Building on this, HI-LLF [29] introduces interleaved interaction units to establish a hierarchical texture base before applying an EPI-specific refinement module. However, these methods often accumulate errors during the initial spatial-angular stages, leading to structural misalignments that are difficult to rectify in subsequent geometric optimization steps.

The cascade paradigm adopts a more fine-grained alternating extraction strategy. Zhang et al. [30] proposed an adaptive feature aggregation (AFA) framework based on cascade residual learning. This approach sequentially cascades inter-intra spatial (II-SFE), inter-intra angular (II-AFE), and horizontal-vertical epipolar feature extractors within each fundamental aggregation block, repeating this process across M aggregation groups. However, the II-SFE and II-AFE modules exhibited high similarity and overlap in feature processing, leading to significant feature redundancy and wasted computation.

Conversely, our proposed RASLF ensures that no redundant information exists between successive refinement steps. Unlike conventional methods that analyze isolated 2D epipolar slices, our approach creates a Panoramic Epipolar Representation to capture global geometric constraints. Consequently, RASLF effectively prevents feature redundancy common in cascaded frameworks and addresses error accumulation common in sequential processing, thereby ensuring strong geometric consistency.

III. METHODOLOGY

A. Overview Architecture

Let $I_{LR} \in \mathbb{R}^{U \times V \times H \times W}$ denote the input low-resolution (LR) LF image, where (U, V) and (H, W) represent the angular and spatial resolutions, respectively. The objective of LFSR is to reconstruct a high-resolution (HR) counterpart $I_{HR} \in \mathbb{R}^{U \times V \times \alpha H \times \alpha W}$, where α denotes the upsampling factor. To effectively restore high-frequency textures while preserving global structural integrity, a residual learning paradigm is adopted. As illustrated in Fig. 1, a global skip connection is established via a bicubic upsampling operator $\mathcal{B}(\cdot)$, yielding the base LF image $I_{\uparrow} = \mathcal{B}(I_{LR}) \in \mathbb{R}^{U \times V \times \alpha H \times \alpha W}$. The network is specifically designed to predict the residual component R , whereby the final super-resolved light field is formulated as $\hat{I}_{HR} = I_{\uparrow} + R$.

The input I_{LR} is first projected into a latent space via a spatial convolution \mathcal{S}_{conv} , followed by a learnable Angular Embedding P_{ang} to encode viewpoint-specific geometric context:

$$F^0 = \mathcal{S}_{conv}(I_{LR}) + P_{ang}, \quad (1)$$

where $F^0 \in \mathbb{R}^{U \times V \times H \times W \times C}$ serves as the initial state for subsequent hierarchical feature extraction.

The backbone of our architecture consists of M cascaded Progressive Geometric Refinement (PGR) blocks for hierarchical spatio-angular feature extraction. Each PGR block applies a sequential transformation across the spatial (SAI), angular (MacPI), and epipolar (EPI) representation domains:

$$F^k = \text{PGR}^k(F^{k-1}), \quad k = 1, \dots, M. \quad (2)$$

This design facilitates step-by-step refinement of spatial textures and angular parallax, leading to a robust, geometrically consistent representation.

Furthermore, a Dual-Anchor Aggregation (DAA) module is developed to generate an aggregated feature representation

F^{agg} . By designating the initial and final cascaded features as spatial and geometric anchors, and adding intermediate layers to enhance residuals, the DAA module reduces hierarchical redundancy while maintaining both spatial accuracy and angular consistency. The total aggregated representation F^* is then generated via a fusion layer:

$$F^* = F^{agg} + F^0. \quad (3)$$

Finally, F^* is processed by a pixel-shuffle upsampling module \mathcal{P}_{sr} to generate the residual R , thereby completing the LF reconstruction. During the training phase, the network is supervised using an L1 loss,

$$\mathcal{L} = \|\hat{I}_{HR} - I_{HR}\|_1. \quad (4)$$

B. Progressive Geometric Refinement

The proposed Progressive Geometric Refinement (PGR) block serves as the basic computational unit for transforming LF representations from low-level spatial textures into high-level geometric constraints. Unlike the common parallel unordered interaction strategies in previous LFSR methods [7], [25], or the sequential architectures that completely decouple spatial-angular interaction from geometric alignment [26]–[28], our method designs a cascade processing chain that explicitly exploits the multi-dimensional physical properties of LF data.

The main motivation is that in traditional sequential architectures, early spatial-angular feature extraction lacks explicit parallax constraints, allowing inconsistent feature responses to spread and accumulate through deep layers. Conversely, the proposed cascaded strategy interleaves refinement across the SAI, MacPI, and EPI domains within each PGR block, enabling "coupling while calibration." Performing real-time geometric calibration at each depth level establishes accurate search benchmarks for feature extraction, effectively reducing visual artifacts caused by matching ambiguities and preventing geometric offsets from accumulating in deeper layers.

To ensure algorithmic consistency and computational efficiency, we adopt the visual state space model (VSSM) proposed in [8] as the base operator, whose effectiveness and efficiency have been well proven on the LFSR task. VSSM enables effective long-range dependency modeling with linear computational complexity, which is essential for processing high-dimensional and redundant LF data. We define the spatial-angular feature extraction process within the PGR block from F^{k-1} to F^k as a generic processor operator $\mathcal{P}(F, \mathcal{T}, \mathcal{T}^{-1}, \Phi)$. Here, $F \in \mathbb{R}^{U \times V \times H \times W \times C}$ denotes the input 4D LF feature tensor, $\mathcal{T}(\cdot)$ and $\mathcal{T}^{-1}(\cdot)$ represent the domain-specific transformation and its inverse, respectively. Φ denotes the predefined set of scanning paths.

Within the specific feature extraction pipeline, the input feature F^{k-1} first undergoes intra-view spatial refinement. The transformation \mathcal{T}_{sai} reshapes the 4D tensor into tiled spatial slices of dimension $(U \cdot V) \times (H \cdot W) \times C$, which are then processed using a domain-specific scanning set Φ_{SAI} . The resulting intermediate spatial-refined feature is expressed as follows:

$$F_{SAI}^{k-1} = \mathcal{P}(F^{k-1}, \mathcal{T}_{SAI}, \mathcal{T}_{SAI}^{-1}, \Phi_{SAI}). \quad (5)$$

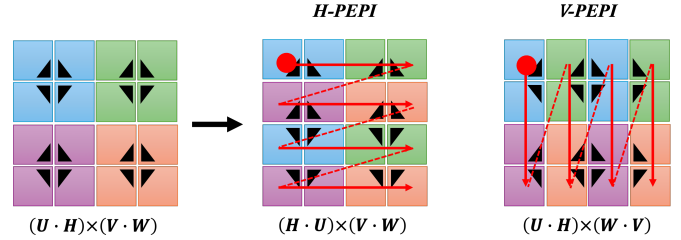


Fig. 2. Illustration of the Panoramic Epipolar Representation and the corresponding representation-aware scanning paths (indicated by red solid arrows).

Subsequently, the feature is reorganized into the MacPI domain via \mathcal{T}_{MAC} , mapping it to a $(H \cdot W) \times (U \cdot V) \times C$ tensor to facilitate angular coupling:

$$F_{MAC}^{k-1} = \mathcal{P}(F_{SAI}^{k-1}, \mathcal{T}_{MAC}, \mathcal{T}_{MAC}^{-1}, \Phi_{MAC}). \quad (6)$$

Through this hierarchical preprocessing, the features are endowed with a robust textural foundation and initial parallax awareness before the geometric alignment stage.

As the key part of the PGR block, the epipolar geometric alignment explicitly enforces the intrinsic linear geometric consistency of the light field. Unlike conventional methods that analyze isolated 2D epipolar slices, our approach develops a Panoramic Epipolar (PEPI) representation to capture global geometric constraints. The composite epipolar transformation \mathcal{T}_{epi} comprises two symmetric reorganization branches: the Vertical Panoramic EPI (V-PEPI), generated via \mathcal{T}_v as a $(H \cdot U) \times (V \cdot W) \times C$ tensor, and the Horizontal Panoramic EPI (H-PEPI), concurrently reshaped via \mathcal{T}_h into a $(W \cdot V) \times (U \cdot H) \times C$ representation (see Fig. 2).

This innovative tiling approach explicitly and effectively maps parallax-related information, originally dispersed in the 4D spatio-angular domain, onto structured 2D planes. This globalized representation allows the processor to not only capture linear slopes within individual epipolar lines but also to observe structural correlations across different spatial locations, utilizing the long-range modeling ability of SSMs. Ultimately, the geometric features are integrated and processed, with the output of the PGR block, F^k , expressed as follows:

$$F^k = \mathcal{T}_{epi}^{-1}(\mathcal{P}(\hat{F}_{mac}, \mathcal{T}_{epi}, \mathcal{T}_{epi}^{-1}, \Phi_{epi})), \quad (7)$$

where $\mathcal{T}_{epi} = \{\mathcal{T}_h, \mathcal{T}_v\}$ and $\Phi_{epi} = \{\Phi_h, \Phi_v\}$.

Compared to the implicit modeling in [8], which scans the angular grid sequentially, our scheme mitigates information decay during long-range state updates and, crucially, circumvents the geometric constraint lag inherent in the "coupling before alignment" sequence of traditional architectures. By jointly characterizing spatial positions and view variations on a unified EPI plane within each block, parallax structures are calibrated in real-time in a more concentrated and explicit manner.

C. Representation-Aware Asymmetric Scanning Strategy

In two-dimensional (2D) image state-space modeling, scanning directions are used to serialize spatial pixels into

sequential state-update paths, capturing directional dependencies. Current methods [31], [32] typically adopt the 2D Selective Scanning (SS2D) mechanism, which employs a quad-directional scanning configuration $\Phi_{4-path} = \{\Phi_{row}, \Phi'_{row}, \Phi_{col}, \Phi'_{col}\}$ across all feature domains, representing forward/inverse row-major and column-major trajectories. However, we argue that applying this quad-directional scanning uniformly across all LF representations ignores their distinct physical priors and introduces unnecessary computational redundancy. To address this issue, we proposed the Representation-Aware Asymmetric Scanning (RAAS) strategy, which dynamically tailors the scanning path set Φ to the physical characteristics of disparate representation domains, achieving an optimal balance between reconstruction performance and computational efficiency through strategic path pruning.

In the intra-view spatial refinement stage, SAI-VSSM aims to capture local spatial dependencies within individual sub-aperture images. Compared with the strong directional structures in MacPI and EPI representations, SAIs exhibit more locally symmetric spatial dependencies, making simple forward scanning sufficient for effective neighborhood correlation modeling. In this case, backward scanning tends to capture largely overlapping contextual dependencies, leading to limited additional benefits while introducing extra computational overhead. Consequently, we implemented a path pruning strategy in SAI-VSSM by retaining only forward state-update paths, i.e., $\Phi_{sai} = \{\Phi_{row}, \Phi_{col}\}$.

Unlike SAI, MacPI interleaves spatial and angular dimensions, such that neighboring elements along each scan axis no longer represent simple local adjacency, but instead reflect coupled relations across different views and spatial positions. As a result, forward and backward scanning propagate context through different dependency chains and capture distinct yet complementary spatial-angular correlations, making bidirectional scanning necessary rather than redundant. Thus, MacPI-VSSM preserves the full quad-directional scanning set, i.e., $\Phi_{mac} = \Phi_{4-path}$, to ensure adequate inter-view correspondence coupling.

The path design for EPI-VSSM is motivated by the strong directional structure of epipolar representations. In our PEPI representation, epipolar trajectories are consistently aligned with the row axis in H-PEPI and the column axis in V-PEPI. Under this formulation, the SSM can effectively propagate parallax-dependent information along these physically meaningful linear paths, making a single forward scan sufficient to capture the dominant geometric dependencies. In contrast, scanning along other directions provides limited additional geometric cues, as they do not follow the principal orientation of epipolar trajectories and mainly introduce redundant context modeling. Therefore, for the decoupled horizontal and vertical branches, we reduce the scanning paths to a single direction $\Phi_{v-epi} = \{\Phi_{col}\}$ and $\Phi_{h-epi} = \{\Phi_{row}\}$, as shown in Fig. 2.

From a computational complexity perspective, the RAAS strategy compresses the structure of the state-space modeling branches by matching the scanning density to the needs of physical modeling. Since each scanning path represents an independent state-update operation, reducing the number of di-

rections directly lowers the parameter count and computational cost. As a result, our method attains greater computational efficiency and stronger geometric consistency representations while still preserving adequate modeling capacity.

D. Dual-Anchor Aggregation Module

In cascaded LFSR architectures, the deliberate integration of hierarchical features is crucial for enhancing reconstruction accuracy. Typically, the evolution of features within these cascaded structures shows a clear functional hierarchy. The shallow features tend to retain the local spatial textures of the original input, whereas deep features, through receptive-field expansion and nonlinear mapping, gradually develop into global representations that incorporate spatial-angular geometric information. To fully utilize these complementary characteristics without creating hierarchical redundancy, we propose the Dual-Anchor Aggregation (DAA) mechanism.

LFSR requires balancing the accuracy of high-frequency details with the stability of angular structures; to achieve this, the DAA module explicitly sets the endpoints of the cascading path as main reference points. Since the initial features F^1 have not undergone extensive abstraction and retain the most intact original spatial details, they are designated as the anchor for spatial texture restoration. Meanwhile, the final features F^M , which integrate spatial-angular geometric constraints, are regarded as the anchor for global geometric modeling.

To enable effective utilization of intermediate feature information within the cascaded sequence $\{F^k\}_{k=2}^{M-1}$, we treat them as adaptive refinement operators. By injecting progressive information from intermediate layers into the boundary anchors through weighted residuals, we constructed enhanced spatial F^S and geometric F^G anchors:

$$F^S = w_1^S \cdot F^1 + \sum_{k=2}^{M-1} w_k^S \cdot F^k, \quad (8)$$

$$F^G = w_M^G \cdot F^M + \sum_{k=2}^{M-1} w_k^G \cdot F^k, \quad (9)$$

Where $\{w_k^S\}_{k=1}^{M-1}$ and $\{w_k^G\}_{k=2}^M$ denote the decoupled weighting coefficients that regulate the contribution of each layer to the respective anchors.

This design enables thorough recovery of feature resources and maximizes effectiveness, thereby improving the texture expressiveness of the spatial anchor and strengthening the structural robustness of the geometric anchor. Subsequently, the DAA module uses dimensional concatenation and a projection layer to achieve deep coupling of these two complementary anchor representations, generating the final aggregated features F^{agg} :

$$F^{agg} = \text{MLP}(\text{Concat}(F^S, F^G)). \quad (10)$$

This anchor-guided aggregation method explicitly removes the hierarchical redundancy caused by cascading schemes at the structural level. Instead of simply concatenating all layers, our approach uses intermediate features as directional refinements, keeping the reconstruction rooted in stable spatial references and accurate geometric benchmarks.

TABLE I
PSNR/SSIM RESULTS COMPARED WITH SOTA METHODS FOR $2\times$ AND $4\times$ LFSR TASKS. THE BEST AND SECOND-BEST RESULTS ARE, RESPECTIVELY, IN BOLD AND UNDERLINED.

Method	Scale	EPFL	HCINew	HCIOld	INRIA	STFgantry	Average
RCAN [33]	$\times 2$	33.156/0.9635	35.022/0.9603	41.125/0.9875	35.036/0.9769	36.670/0.9831	36.202/0.9743
resLF [34]	$\times 2$	33.617/0.9706	36.685/0.9739	43.422/0.9932	35.395/0.9804	38.354/0.9904	37.495/0.9817
LFSSR [35]	$\times 2$	33.671/0.9744	36.802/0.9749	43.811/0.9938	35.279/0.9832	37.944/0.9898	37.501/0.9832
LF-ATO [36]	$\times 2$	34.272/0.9757	37.244/0.9767	44.205/0.9942	36.171/0.9842	39.636/0.9929	38.306/0.9847
MEG-Net [37]	$\times 2$	34.312/0.9773	37.424/0.9777	44.097/0.9942	36.103/0.9849	38.767/0.9915	38.141/0.9851
DistgSSR [25]	$\times 2$	34.809/0.9787	37.959/0.9796	44.943/0.9949	36.586/0.9859	40.404/0.9942	38.940/0.9867
LF-InterNet [38]	$\times 2$	34.112/0.9760	37.170/0.9763	44.573/0.9946	35.829/0.9843	38.435/0.9909	38.024/0.9844
LF-IIINet [39]	$\times 2$	34.736/0.9773	37.768/0.9790	44.852/0.9948	36.564/0.9853	39.894/0.9936	38.763/0.9860
HLFSR-SSR [40]	$\times 2$	35.310/0.9800	38.317/0.9807	44.978/0.9950	37.060/0.9867	40.849/0.9947	39.303/0.9874
DPT [21]	$\times 2$	34.490/0.9758	37.355/0.9771	44.302/0.9943	36.409/0.9843	39.429/0.9926	38.397/0.9848
LFT [20]	$\times 2$	34.783/0.9776	37.766/0.9788	44.628/0.9947	36.539/0.9853	40.408/0.9941	38.825/0.9861
EPIT [24]	$\times 2$	34.826/0.9775	38.228/0.9810	45.075/0.9949	36.672/0.9853	42.166/0.9957	39.393/0.9869
LF-DET [18]	$\times 2$	35.262/0.9797	38.314/0.9807	44.986/0.9950	36.949/0.9864	41.762/0.9855	39.455/0.9874
MLFSR [6]	$\times 2$	35.218/0.9801	38.140/0.9803	44.904/0.9950	36.919/0.9865	40.975/0.9949	39.231/0.9873
LFMamba [7]	$\times 2$	35.758/0.9824	38.368/0.9801	44.985/0.9950	<u>37.063/0.9876</u>	40.954/0.9948	39.424/0.9881
L^2 FMamba [8]	$\times 2$	35.515/0.9796	38.225/0.9803	44.953/0.9949	37.165/0.9862	41.567/0.9952	39.485/0.9873
RASLF (Our)	$\times 2$	35.176/0.9791	38.427/0.9813	45.312/0.9952	36.987/0.9861	<u>41.873/0.9955</u>	39.555/0.9875
RCAN [33]	$\times 4$	27.904/0.8863	29.694/0.8886	35.359/0.9548	29.800/0.9276	29.021/0.9131	30.355/0.9141
resLF [34]	$\times 4$	28.260/0.9035	30.723/0.9107	36.705/0.9682	30.338/0.9412	30.191/0.9372	31.243/0.9322
LFSSR [35]	$\times 4$	28.596/0.9118	30.928/0.9145	36.907/0.9696	30.585/0.9467	30.570/0.9426	31.517/0.9370
LF-ATO [36]	$\times 4$	28.514/0.9115	30.880/0.9135	36.999/0.9699	30.710/0.9484	30.607/0.9430	31.542/0.9373
MEG-Net [37]	$\times 4$	28.749/0.9160	31.103/0.9177	37.287/0.9716	30.674/0.9490	30.771/0.9453	31.717/0.9399
DistgSSR [25]	$\times 4$	28.992/0.9195	31.380/0.9217	37.563/0.9732	30.994/0.9519	31.649/0.9534	32.116/0.9439
LF-InterNet [38]	$\times 4$	28.812/0.9162	30.961/0.9161	37.150/0.9716	30.777/0.9491	30.365/0.9409	31.613/0.9388
LF-IIINet [39]	$\times 4$	29.048/0.9188	31.331/0.9208	37.620/0.9734	31.039/0.9515	31.261/0.9502	32.060/0.9429
HLFSR-SSR [40]	$\times 4$	29.196/0.9222	31.571/0.9238	37.776/0.9742	31.241/0.9543	31.641/0.9537	32.285/0.9456
DPT [21]	$\times 4$	28.939/0.9170	31.196/0.9188	37.412/0.9721	30.964/0.9503	31.150/0.9488	31.932/0.9414
LFT [20]	$\times 4$	29.261/0.9209	31.433/0.9215	37.633/0.9735	31.218/0.9524	31.794/0.9543	32.268/0.9445
EPIT [24]	$\times 4$	29.339/0.9197	31.511/0.9231	37.677/0.9737	31.372/0.9526	32.179/0.9571	32.416/0.9452
LF-DET [18]	$\times 4$	29.473/0.9230	31.558/0.9235	37.843/0.9744	31.388/0.9534	32.139/0.9573	32.480/0.9463
MLFSR [6]	$\times 4$	29.283/0.9218	31.564/0.9235	37.831/0.9745	31.241/0.9531	32.031/0.9567	32.389/0.9235
LFMamba [7]	$\times 4$	29.840/0.9256	31.695/0.9249	37.912/0.9748	31.808/0.9551	31.846/0.9553	32.620/0.9471
L^2 FMamba [8]	$\times 4$	29.681/0.9233	31.647/0.9243	37.864/0.9745	31.728/0.9543	<u>32.198/0.9574</u>	<u>32.623/0.9468</u>
RASLF (Our)	$\times 4$	<u>29.763/0.9239</u>	<u>31.667/0.9245</u>	<u>37.894/0.9745</u>	<u>31.758/0.9544</u>	32.368/0.9586	32.690/0.9472

IV. EXPERIMENTS

A. Datasets and Implementation Details

To comprehensively evaluate the effectiveness of RASLF, we conducted experiments on three real-world LF datasets, EPFL [41], INRIA [42], and STF-gantry [43], as well as two synthetic LF datasets, HCIOld [44], and HCINew [45]. For all datasets, we strictly followed the publicly available data splitting protocols and pre-processing procedures adopted in prior work to ensure fair and reproducible comparisons. Specifically, we used the central 5×5 views of each LF image and cropped HR patches from these views for both training and testing. HR patches are cropped with sizes of 64×64 and 128×128 for the $2\times$ and $4\times$ LFSSR tasks, respectively. The corresponding LR inputs are generated via bicubic down-sampling, yielding LR patches of size 32×32 . For quantitative evaluation, we converted the LF images from RGB to YCbCr and computed the peak signal-to-noise ratio (PSNR) and structural similarity (SSIM) on the Y channel only. For each dataset, we first averaged the metrics across all LF scenes, then averaged the results across the five datasets to obtain the final scores.

To facilitate the RAAS strategy while avoiding sub-optimal convergence inherent in training sparse architectures from scratch, a two-stage training paradigm is adopted. First, a full-

path model is pre-trained for 180 epochs to capture dense feature representations. We used the Adam optimizer and a StepLR scheduler, with an initial learning rate of $2e-4$ that is decreased by a factor of 0.5 every 30 epochs. The training data is augmented with random horizontal and vertical flips and 90-degree rotations. Subsequently, guided by the RAAS strategy, redundant scanning paths are pruned according to the representation-specific requirements, as defined in Sec. III-C. The pruned model is then fine-tuned for 30 epochs with a learning rate of $5e-5$, which is decayed by a factor of 0.5 every 15 epochs to smoothly recover and optimize the final performance.

B. Comparisons with State-of-The-Art Methods

To thoroughly assess the proposed RASLF, we compared it against 16 representative state-of-the-art methods across quantitative metrics, visual quality, and computational efficiency. The compared methods cover both SISR and LFSR tasks. Specifically, RCAN [33] serves as the CNN-based SISR method. For LFSR, DPT [21], [20], EPIT [24], and LF-DET [18] are built upon Transformer architectures, whereas LFMamba [7], L^2 FMamba [8], and MLFSR [6] adopt state-space structures. The remaining approaches are based on CNN

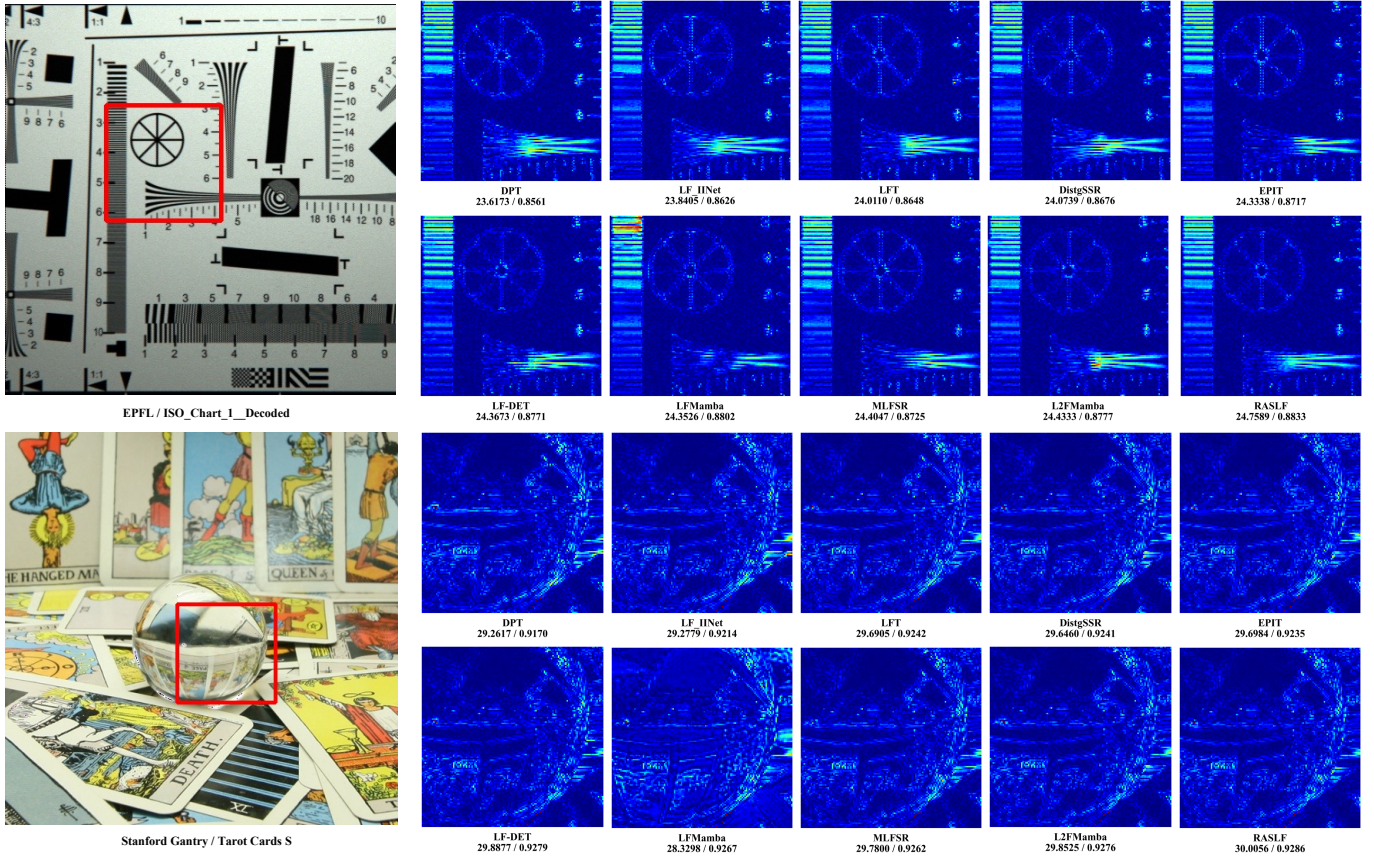


Fig. 3. Qualitative visualization results for $4\times$ LFSR compared to other methods. Here, we showed the error maps of the reconstructed center-view images, with representative regions indicated by arrows. PSNR/SSIM values for the corresponding region are provided below.

TABLE II
COMPARISON OF PARAMETERS, FLOPS, TIME, AND AVERAGE PSNR/SSIM VALUES FOR $\times 2$ AND $\times 4$ SR. FLOPS AND TIME ARE CALCULATED ON AN INPUT LF WITH A SIZE OF $5 \times 5 \times 32 \times 32$.

Method	Scale	Params.	FLOPs(G)	Time(ms)	Avg. PSNR/SSIM
LFSSR [35]	$\times 2$	0.89M	25.70	10.0	37.501/0.9832
MEG-Net [37]	$\times 2$	1.69M	48.40	31.2	38.141/0.9851
LF-ATO [36]	$\times 2$	1.22M	597.66	85.6	38.306/0.9847
LF-IINet [39]	$\times 2$	5.04M	56.16	20.6	38.763/0.9860
DistgSSR [25]	$\times 2$	3.53M	64.11	24.2	38.940/0.9867
HLFSR-SSR [40]	$\times 2$	13.72M	167.81	31.1	39.303/0.9874
LFT [20]	$\times 2$	1.11M	56.16	91.4	38.825/0.9861
DPT [21]	$\times 2$	3.73M	65.34	98.5	38.397/0.9848
EPIT [24]	$\times 2$	1.42M	69.71	32.2	39.393/0.9869
LF-DET [18]	$\times 2$	1.59M	48.50	65.9	39.455/0.9874
MLFSR [6]	$\times 2$	1.36M	53.30	27.8	39.231/0.9873
LFMamba [7]	$\times 2$	2.15M	92.29	75.9	39.424/0.9881
L^2 FMamba [8]	$\times 2$	1.04M	36.59	31.9	39.485/0.9873
RASLF (Our)	$\times 2$	0.90M	29.77	28.8	39.552/0.9876

Method	Scale	Params.	FLOPs(G)	Time(ms)	Avg. PSNR/SSIM
LFSSR [35]	$\times 4$	1.61M	128.44	37.7	31.517/0.9370
MEG-Net [37]	$\times 4$	1.77M	102.20	32.4	31.717/0.9399
LF-ATO [36]	$\times 4$	1.66M	686.99	88.7	31.542/0.9373
LF-IINet [39]	$\times 4$	4.89M	57.42	20.8	32.060/0.9429
DistgSSR [25]	$\times 4$	3.58M	65.41	25.0	32.116/0.9439
HLFSR-SSR [40]	$\times 4$	13.87M	182.93	32.7	32.285/0.9456
LFT [20]	$\times 4$	1.16M	57.60	95.2	32.268/0.9445
DPT [21]	$\times 4$	3.78M	66.55	99.7	31.932/0.9414
EPIT [24]	$\times 4$	1.47M	71.15	33.6	32.416/0.9452
LF-DET [18]	$\times 4$	1.69M	51.20	75.0	32.480/0.9463
MLFSR [6]	$\times 4$	1.41M	54.74	28.9	32.389/0.9235
LFMamba [7]	$\times 4$	2.30M	96.24	77.1	32.620/0.9471
L^2 FMamba [8]	$\times 4$	1.09M	37.99	32.6	32.623/0.9468
RASLF (Our)	$\times 4$	0.95M	31.20	29.4	32.690/0.9472

architectures, including LFSSR [35], MEG-Net [37], LF-ATO [36], LF-IINet [39], DistgSSR [25], and HLFSR-SSR [40].

1) *Quantitative Results:* The quantitative comparisons between RASLF and other state-of-the-art methods are presented in Table I. In the $4\times$ LFSR task, RASLF achieves the best performance across all datasets, consistently outperforming the efficient state-space baseline L^2 FMamba. Notably, on the STF-gantry dataset, which features large-scale parallax, RASLF surpasses L^2 FMamba by 0.17 dB and LFMamba by 0.52 dB. This significant improvement confirms that our PGR block effectively enforces explicit geometric calibration

on panoramic representations, enabling precise modeling of complex cross-view dependencies. In the $2\times$ LFSR task, RASLF remains highly competitive, achieving the highest average PSNR among all methods. Although LFMamba achieves a slightly higher SSIM, RASLF still outperforms its direct competitor, L^2 FMamba, in both PSNR and SSIM. Considering the extremely low parameter count of RASLF, these results indicate that our method achieves a favorable balance between pixel-level fidelity and geometric consistency while maintaining efficient inference.

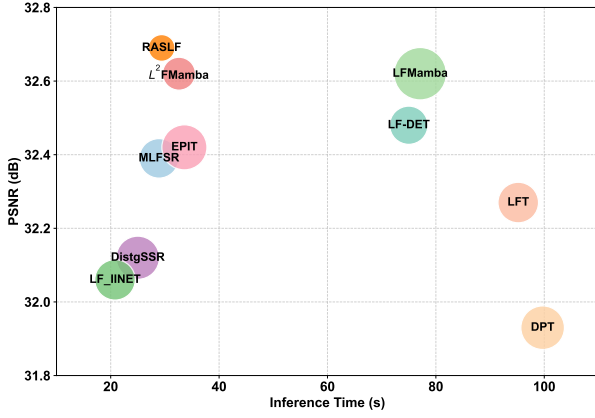


Fig. 4. Comparison of computational efficiency between our method and SOTA models on the $4\times$ LFSR task. The area of each circle represents memory consumption.

TABLE III
ABLATION STUDY ON DIFFERENT COMPONENTS FOR $4\times$ LFSR.

	PSNR / SIMM	Params	FLOPs
w/o. DDA	32.637 / 0.9466	1.086	37.928
w. EPI-H & EPI-V	32.588 / 0.9466	0.953	31.200
w. EPIs-H & EPIs-V	32.628 / 0.9468	0.953	31.200
RASLF (Our)	32.690 / 0.9472	0.953	31.200

2) *Qualitative Results*: Fig. 3 presents the qualitative results of error maps for different methods on the $4\times$ LFSR task. Compared with other state-of-the-art methods, our approach shows better ability to restore texture details and maintain structural consistency. This is primarily attributed to our proposed PGR block and Panoramic Epipolar Representation, which jointly reorganize fragmented local epipolar constraints into a globally coherent geometric structure, as evidenced by the significantly lower error responses. In varied and challenging scenes, such as the dense radial lines in "EPFL/ISO_Chart_1_Decoded" and the complex specular reflections and distinct contours of the crystal ball in "Stanford Gantry/Tarot Cards S", our method achieves outstanding performance, producing the cleanest error maps. In particular, compared to recent SSM-based architectures such as LFMamba and L^2 FMamba, our proposed RASLF achieves more visually pleasing error suppression and superior quantitative results.

3) *Computational Efficiency*: We compared RASLF with representative existing methods under standardized conditions in terms of model complexity, including the number of parameters (Params.), floating-point operations (FLOPs), and inference time (Time). For the LFSR task, all methods took LF patches of size $5 \times 5 \times 32 \times 32$ as input and are evaluated on a unified NVIDIA RTX 3090 GPU hardware platform, covering both $\times 2$ and $\times 4$ SR scales. Quantitative efficiency metrics in Table II reveal that RASLF achieves a superior trade-off between model complexity and accuracy.

Specifically, compared to Transformer-based methods, RASLF significantly lowers computational costs and provides

much faster inference. Although its inference speed is slightly lower than that of lightweight CNN-based methods, it remains highly competitive regarding overall efficiency. Notably, current state-space model implementations are not yet as heavily optimized for GPUs as convolutional operators; therefore, with continued development of hardware-aware SSM operators, the inference efficiency of RASLF is expected to improve further.

Compared with MLFSR and LFMamba, RASLF achieves higher reconstruction accuracy with fewer parameters, lower computational complexity, and shorter inference time. Furthermore, even compared with the state-of-the-art efficiency-oriented model L^2 FMamba, which adopts a similar VSSM backbone, RASLF maintains a clear advantage. Specifically, at the $4\times$ scale, RASLF achieves a 12.8% reduction in parameter scale and a 17.9% reduction in FLOPs compared to L^2 FMamba, while also improving the PSNR by 0.07 dB. This shows that pruning strategic paths in our RAAS approach effectively removes unnecessary calculations without losing representational capability.

To evaluate runtime efficiency and resource usage, we compared the inference time and GPU memory consumption between our method and SOTA models on the $4\times$ LFSR task in Fig. 4. The area of each circle indicates peak memory usage. Our proposed RASLF achieves a superior balance between reconstruction performance and computational cost. By effectively pruning hierarchical and directional redundancies, our framework maximizes resource utilization for critical reconstruction information.

C. Ablation Study

1) *Dual-Anchor Aggregation Module*: To verify the effectiveness of the Dual-Anchor Aggregation (DAA) module in hierarchical feature fusion, we evaluate a variant in which the DAA is replaced with a simple feature concatenation operation, denoted w/o DAA. As reported in Table III, removing DDA increases the parameter count by about 14.0% and raises FLOPs by about 21.6%, while the reconstruction accuracy decreases by 0.05 dB in PSNR. This contrast confirms that simple hierarchical stacking introduces significant hierarchical redundancy, whereas the DAA effectively improves feature utilization and reduces model complexity through an anchor-guided mechanism.

2) *Panoramic Epipolar Representation*: We further investigated the impact of different epipolar representations on reconstruction performance. While keeping the rest of the network fixed, the Panoramic Epipolar Representation (PER) is compared against conventional isolated epipolar slices (w. EPI) and stacked epipolar slices (w. EPIs).

As shown in Table III, the configuration with isolated EPI slices delivers the lowest reconstruction accuracy, achieving a PSNR of 32.588 dB. This is because fragmented slices interrupt the geometric continuity of the light field, preventing the capture and transmission of global disparity dependencies. While stacking EPIs partially alleviates this issue and improves PSNR to 32.628 dB, it still lags behind the PEPI-based final configuration. By creating a continuous panoramic epipolar plane, PEPI more effectively preserves global geometric structures, thereby providing higher-quality reconstruction.

TABLE IV
ABLATION STUDY ON DIFFERENT REPRESENTATION SCANNING STRATEGIES FOR $4 \times$ LFSR.

	SAI	MacPI	H-EPI	V-EPI	PSNR / SIMM	Params	FLOPS
(a)	Φ_{4-path}	Φ_{4-path}	$\{\Phi_{row}, \Phi'_{row}\}$	$\{\Phi_{col}, \Phi'_{col}\}$	32.703 / 0.9473	1.013	36.050
(b)	$\{\Phi_{row}, \Phi_{col}\}$	Φ_{4-path}	$\{\Phi_{row}, \Phi'_{row}\}$	$\{\Phi_{col}, \Phi'_{col}\}$	32.700 / 0.9471	0.983	33.625
(c)	$\{\Phi_{row}, \Phi_{col}\}$	Φ_{4-path}	$\{\Phi_{col}\}$	$\{\Phi_{col}\}$	32.696 / 0.9471	0.953	31.200
(d)	$\{\Phi_{row}, \Phi_{col}\}$	$\{\Phi_{row}, \Phi_{col}\}$	$\{\Phi_{col}\}$	$\{\Phi_{col}\}$	32.329 / 0.9440	0.923	28.775

TABLE V
INVESTIGATION ON THE SCALABILITY OF THE PROPOSED RASLF WITH RESPECT TO NETWORK DEPTH (NUMBER OF PGR BLOCKS M) AND WIDTH (FEATURE DIMENSIONS C).

M	C	PSNR / SIMM	Params	FLOPS
4	64	32.690 / 0.9472	0.953	31.200
8	64	32.901 / 0.9492	1.654	55.756
12	64	32.972 / 0.9497	2.310	76.676
16	64	33.070 / 0.9502	2.996	100.020
4	128	33.039 / 0.9498	3.486	101.185
4	256	33.129 / 0.9508	13.412	367.205

Notably, these three variants have identical parameter scales and computational costs, confirming that the benefits of PER arise solely from improved representational ability rather than from increased model capacity.

3) Representation-Aware Asymmetric Scanning Strategy:

To validate the Representation-Aware Asymmetric Scanning (RAAS) strategy, we conduct a quantitative ablation on scanning configurations for the $4 \times$ LFSR task, as summarized in Table IV. Exp. (a) serves as the symmetric-scanning baseline, employing quad-directional state updates following the standard SS2D design. Exp. (b) applies RAAS exclusively to the SAI branch; pruning the inverse trajectories reduces FLOPs by 6.7% with negligible performance impact. This indicates that inverse paths provide limited additional benefits in spatial domains with locally symmetric dependencies. Exp. (c) extends RAAS to the EPI domain by pruning to a single epipolar-aligned traversal, while preserving full coupling in MacPI. This achieves a 13.5% reduction in FLOPs relative to Exp. (a) without noticeable degradation. Conversely, Exp. (d) additionally prunes the MacPI paths, resulting in a clear drop in accuracy. This suggests that the MacPI domain necessitates comprehensive directional coupling to support complex mixed spatial-angular interactions, and that excessive pruning hinders effective cross-view information propagation.

D. Model Scaling Analysis

To evaluate the scalability of RASLF, we investigated the impact of network depth (number of PGR blocks, M) and width (feature dimension, C) on the performance-efficiency trade-off. As shown in Table V, increasing M from 4 to 16 with a fixed $C = 64$ consistently improves performance with linear growth in complexity, confirming the effectiveness of the DAA module in reducing redundancy in deep architectures.

Notably, a comparison between configurations with similar Flops, specifically the deeper variant ($M = 16, C = 64$)

and the wider variant ($M = 4, C = 128$), shows that increasing cascading depth is more effective than expanding feature dimensionality. The former achieves higher accuracy with a more compact parameter footprint, providing empirical evidence that depth-wise cascading is more critical than width-wise expansion for efficient light-field modeling. This cascaded structure facilitates the continuous refinement of geometric representations through iterative state-space evolutions. Conversely, expanding the feature dimension to 256 leads to a disproportionate increase in parameters and FLOPs, with diminishing marginal utility. Therefore, to achieve the best balance between accuracy and computational cost, the configuration of $M = 4$ and $C = 64$ is chosen as the standard RASLF baseline.

V. CONCLUSION

This study presented RASLF, a representation-aware state space framework designed to facilitate deep collaboration among diverse LF representations. By integrating Progressive Geometric Refinement (PGR) with a Panoramic Epipolar Representation (PEPI), the proposed method successfully ensures global geometric consistency. Furthermore, the Representation-Aware Asymmetric Scanning (RAAS) strategy and the Dual-Anchor Aggregation (DAA) module effectively eliminate directional and hierarchical redundancies, respectively, thereby improving the balance between reconstruction accuracy and computational efficiency. Extensive evaluations on five public benchmarks confirmed that RASLF achieves state-of-the-art (SOTA) performance with remarkably compact parameters.

Future research will investigate the integration of light-field geometric priors with the intermediate states of the state-space model, promoting synergistic representations between SSM and LF features to further improve cross-view consistency and high-frequency texture restoration.

REFERENCES

- [1] Z. Cui, H. Sheng, D. Yang, S. Wang, R. Chen, and W. Ke, "Light field depth estimation for non-lambertian objects via adaptive cross operator," *IEEE Transactions on Circuits and Systems for Video Technology*, vol. 34, no. 2, pp. 1199–1211, 2024.
- [2] W. Chao, F. Duan, X. Wang, Y. Wang, K. Lu, and G. Wang, "Occasnet: Occlusion-aware cascade cost volume for light field depth estimation," *IEEE Transactions on Computational Imaging*, vol. 10, pp. 1680–1691, 2024.
- [3] Y. Yang, L. Wu, L. Zeng, T. Yan, and Y. Zhan, "Joint upsampling for refocusing light fields derived with hybrid lenses," *IEEE Transactions on Instrumentation and Measurement*, vol. 72, pp. 1–12, 2023.
- [4] X. Ban, Y. Liu, L. Zhang, and Z. Fan, "Focus-aware fusion for enhanced all-in-focus light field image generation," *IEEE Transactions on Instrumentation and Measurement*, vol. 73, pp. 1–18, 2024.

- [5] Z. Chen and E. N. Brown, "State space model," *Scholarpedia*, vol. 8, no. 3, p. 30868, 2013.
- [6] R. Gao, Z. Xiao, and Z. Xiong, "Mamba-based light field super-resolution with efficient subspace scanning," in *Proceedings of the Asian Conference on Computer Vision (ACCV)*, December 2024, pp. 531–547.
- [7] W. xia, Y. Lu, S. Wang, Z. Wang, P. Xia, and T. Zhou, "Lfmamba: Light field image super-resolution with state space model," 2024. [Online]. Available: <https://arxiv.org/abs/2406.12463>
- [8] Z. Wei, K. Jin, Z. Hou, K. Song, and X. Zhou, " l^2 fmamba: Lightweight light field image super-resolution with state space model," *IEEE Transactions on Computational Imaging*, vol. 11, pp. 816–826, 2025.
- [9] X. Pei, T. Huang, and C. Xu, "Efficientvmamba: Atrous selective scan for light weight visual mamba," *Proceedings of the AAAI Conference on Artificial Intelligence*, vol. 39, no. 6, pp. 6443–6451, Apr. 2025.
- [10] H. Xiao, L. Tang, P.-T. Jiang, H. Zhang, J. Chen, and B. Li, "Boosting vision state space model with fractal scanning," in *Proceedings of the Thirty-Ninth AAAI Conference on Artificial Intelligence and Thirty-Seventh Conference on Innovative Applications of Artificial Intelligence and Fifteenth Symposium on Educational Advances in Artificial Intelligence*. AAAI Press, 2025.
- [11] H. Guo, Y. Guo, Y. Zha, Y. Zhang, W. Li, T. Dai, S.-T. Xia, and Y. Li, "Mambairv2: Attentive state space restoration," in *Proceedings of the IEEE/CVF Conference on Computer Vision and Pattern Recognition (CVPR)*, June 2025, pp. 28 124–28 133.
- [12] M. Levoy and P. Hanrahan, "Light field rendering," ser. SIGGRAPH '96. Association for Computing Machinery, 1996, p. 31–42.
- [13] R. C. Bolles, H. H. Baker, and D. H. Marimont, "Epipolar-plane image analysis: An approach to determining structure from motion," *International Journal of Computer Vision*, vol. 1, pp. 7–55, 1987. [Online]. Available: <https://api.semanticscholar.org/CorpusID:12598541>
- [14] Y. Yoon, H.-G. Jeon, D. Yoo, J.-Y. Lee, and I. S. Kweon, "Light-field image super-resolution using convolutional neural network," *IEEE Signal Processing Letters*, vol. 24, no. 6, pp. 848–852, 2017.
- [15] Y. Wang, F. Liu, K. Zhang, G. Hou, Z. Sun, and T. Tan, "Lfnet: A novel bidirectional recurrent convolutional neural network for light-field image super-resolution," *IEEE Transactions on Image Processing*, vol. 27, no. 9, pp. 4274–4286, 2018.
- [16] Y. Wang, L. Wang, J. Yang, W. An, J. Yu, and Y. Guo, "Spatial-angular interaction for light field image super-resolution," in *Computer Vision – ECCV 2020: 16th European Conference, Glasgow, UK, August 23–28, 2020, Proceedings, Part XXIII*. Berlin, Heidelberg: Springer-Verlag, 2020, p. 290–308. [Online]. Available: https://doi.org/10.1007/978-3-030-58592-1_18
- [17] Y. Wang, J. Yang, L. Wang, X. Ying, T. Wu, W. An, and Y. Guo, "Light field image super-resolution using deformable convolution," *IEEE Transactions on Image Processing*, vol. 30, pp. 1057–1071, 2021.
- [18] R. Cong, H. Sheng, D. Yang, Z. Cui, and R. Chen, "Exploiting spatial and angular correlations with deep efficient transformers for light field image super-resolution," *IEEE Transactions on Multimedia*, 2023.
- [19] N. Meng, H. K.-H. So, X. Sun, and E. Y. Lam, "High-dimensional dense residual convolutional neural network for light field reconstruction," *IEEE Transactions on Pattern Analysis and Machine Intelligence*, vol. 43, no. 3, pp. 873–886, 2021.
- [20] Z. Liang, Y. Wang, L. Wang, J. Yang, and S. Zhou, "Light field image super-resolution with transformers," *IEEE Signal Processing Letters*, vol. 29, pp. 563–567, 2022.
- [21] S. Wang, T. Zhou, Y. Lu, and H. Di, "Detail-preserving transformer for light field image super-resolution," in *Proceedings of the AAAI conference on artificial intelligence*, vol. 36, no. 3, 2022, pp. 2522–2530.
- [22] Z. Z. Hu, X. Chen, V. Y. Y. Chung, and Y. Shen, "Beyond subspace isolation: many-to-many transformer for light field image super-resolution," *IEEE Transactions on Multimedia*, 2024.
- [23] K. Jin, Z. Wei, A. Yang, D. Wu, M. Gao, and X. Zhou, "Lfransmamba: A hybrid mamba-transformer model for light field image super-resolution," in *2025 IEEE/CVF Conference on Computer Vision and Pattern Recognition Workshops (CVPRW)*, 2025, pp. 1186–1195.
- [24] Z. Liang, Y. Wang, L. Wang, J. Yang, S. Zhou, and Y. Guo, "Learning non-local spatial-angular correlation for light field image super-resolution," in *Proceedings of the IEEE/CVF International Conference on Computer Vision (ICCV)*, 2023, pp. 12 376–12 386.
- [25] Y. Wang, L. Wang, G. Wu, J. Yang, W. An, J. Yu, and Y. Guo, "Disentangling light fields for super-resolution and disparity estimation," *IEEE Transactions on Pattern Analysis and Machine Intelligence*, vol. 45, no. 1, pp. 425–443, 2022.
- [26] Z. Wang, Y. Lu, S. Wang, W. Xia, P. Xia, and W. Wang, "Trident transformer for light field image super-resolution," in *2024 IEEE International Conference on Multimedia and Expo (ICME)*, 2024, pp. 1–6.
- [27] D. Ke, Y. Chen, C. Jin, H. Xu, Z. Jiang, T. Luo, and G. Jiang, "Combining independent and joint spatial-angular information learning for light field image super-resolution," *Knowledge-Based Systems*, vol. 330, p. 114619, 2025. [Online]. Available: <https://www.sciencedirect.com/science/article/pii/S0950705125016582>
- [28] M. Yu, Z. Wu, and D. Huang, "Lfmix: A lightweight hybrid architecture for light field super-resolution," in *2025 IEEE/CVF Conference on Computer Vision and Pattern Recognition Workshops (CVPRW)*, 2025, pp. 1441–1450.
- [29] M. Li, B. Ma, and S. Wang, "Hierarchical spatial-angular integration for lightweight light field image super-resolution," *Knowledge-Based Systems*, vol. 315, p. 113240, 2025.
- [30] H. Zhang, W. Zhou, L. Lin, and A. Lumsdaine, "Cascade residual learning based adaptive feature aggregation for light field super-resolution," *Pattern Recognition*, vol. 165, p. 111616, 2025.
- [31] Y. Liu, Y. Tian, Y. Zhao, H. Yu, L. Xie, Y. Wang, Q. Ye, J. Jiao, and Y. Liu, "Vmamba: Visual state space model," *Advances in neural information processing systems*, vol. 37, pp. 103 031–103 063, 2024.
- [32] H. Guo, J. Li, T. Dai, Z. Ouyang, X. Ren, and S.-T. Xia, "Mambair: A simple baseline for image restoration with state-space model," in *European conference on computer vision*. Springer, 2024, pp. 222–241.
- [33] Y. Zhang, K. Li, K. Li, L. Wang, B. Zhong, and Y. Fu, "Image super-resolution using very deep residual channel attention networks," in *Proceedings of the European conference on computer vision (ECCV)*, 2018, pp. 286–301.
- [34] S. Zhang, Y. Lin, and H. Sheng, "Residual networks for light field image super-resolution," in *Proceedings of the IEEE/CVF conference on computer vision and pattern recognition*, 2019, pp. 11 046–11 055.
- [35] H. W. F. Yeung, J. Hou, X. Chen, J. Chen, Z. Chen, and Y. Y. Chung, "Light field spatial super-resolution using deep efficient spatial-angular separable convolution," *IEEE Transactions on Image Processing*, vol. 28, no. 5, pp. 2319–2330, 2018.
- [36] J. Jin, J. Hou, J. Chen, and S. Kwong, "Light field spatial super-resolution via deep combinatorial geometry embedding and structural consistency regularization," in *Proceedings of the IEEE/CVF conference on computer vision and pattern recognition*, 2020, pp. 2260–2269.
- [37] S. Zhang, S. Chang, and Y. Lin, "End-to-end light field spatial super-resolution network using multiple epipolar geometry," *IEEE Transactions on Image Processing*, vol. 30, pp. 5956–5968, 2021.
- [38] Y. Wang, L. Wang, J. Yang, W. An, J. Yu, and Y. Guo, "Spatial-angular interaction for light field image super-resolution," in *Computer Vision–ECCV 2020: 16th European Conference, Glasgow, UK, August 23–28, 2020, Proceedings, Part XXIII 16*. Springer, 2020, pp. 290–308.
- [39] G. Liu, H. Yue, J. Wu, and J. Yang, "Intra-inter view interaction network for light field image super-resolution," *IEEE Transactions on Multimedia*, vol. 25, pp. 256–266, 2021.
- [40] V. V. Duong, T. H. Nguyen, J. Yim, and B. Jeon, "Light field image super-resolution network via joint spatial-angular and epipolar information," *IEEE Trans. Computational Imaging*, 2023.
- [41] M. Rerabek and T. Ebrahimi, "New light field image dataset," in *8th International Conference on Quality of Multimedia Experience (QoMEX)*, 2016, pp. 1–2.
- [42] M. Le Pendu, X. Jiang, and C. Guillemot, "Light field inpainting propagation via low rank matrix completion," *IEEE Transactions on Image Processing*, vol. 27, no. 4, pp. 1981–1993, 2018.
- [43] V. Vaish and A. Adams, "The (new) stanford light field archive," *Computer Graphics Laboratory, Stanford University*, vol. 6, no. 7, p. 3, 2008.
- [44] S. Wanner, S. Meister, and B. Goldluecke, "Datasets and benchmarks for densely sampled 4d light fields," in *VMV*, vol. 13, 2013, pp. 225–226.
- [45] K. Honauer, O. Johannsen, D. Kondermann, and B. Goldluecke, "A dataset and evaluation methodology for depth estimation on 4d light fields," in *Computer Vision–ACCV 2016: 13th Asian Conference on Computer Vision, Taipei, Taiwan, November 20–24, 2016, Revised Selected Papers, Part III 13*. Springer, 2017, pp. 19–34.